Observation of a $\bar{K}NN$ bound state in the ^{3}He$(K^-, \Lambda p)n$ reaction

T. Yamaga,[1,*] S. Ajimura,[2] H. Asano,[1] G. Beer,[3] H. Bhang,[4] M. Bragadireanu,[5] P. Buehler,[6] L. Busso,[7,8] M. Cargnelli,[6] S. Choi,[4] C. Curceanu,[9] S. Enomoto,[14] H. Fujioka,[15] Y. Fujiwara,[12] T. Fukuda,[13] C. Guaraldo,[9] T. Hashimoto,[20] R. S. Hayano,[12] T. Hiraiwa,[2] M. Iio,[14] M. Iliescu,[9] K. Inoue,[2] Y. Ishiguro,[11] T. Ishikawa,[12] S. Ishimoto,[14] K. Itahashi,[1] M. Iwai,[14] M. Iwasaki,[1,†] K. Kanno,[12] K. Kato,[11] Y. Kato,[1] S. Kawasaki,[10] P. Kienle,[16,‡] H. Kou,[15] Y. Ma,[1] J. Marton,[6] Y. Matsuda,[17] Y. Mizoi,[13] O. Morra,[7] T. Nagae,[11] H. Noumi,[2,14] H. Ohnishi,[22] S. Okada,[23] H. Outa,[1] K. Piscicchia,[24,9] Y. Sada,[22] A. Sakaguchi,[10] F. Sakuma,[1] M. Sato,[14] A. Scordo,[9] M. Sekimoto,[14] H. Shi,[6] K. Shirotori,[2] D. Sirghi,[9,5] F. Sirghi,[9,5] S. Suzuki,[14] T. Suzuki,[12] K. Tanida,[20] H. Tatsuno,[21] M. Tokuda,[15] D. Tomono,[2] A. Toyoda,[14] K. Tsukada,[18] O. Vazquez Doce,[9,16] E. Widmann,[6] T. Yamazaki,[12,1] H. Yim,[19] Q. Zhang,[1] and J. Zmeskal[6]

(J-PARC E15 Collaboration)

[1]*RIKEN Cluster for Pioneering Research, RIKEN, Wako 351-0198, Japan*
[2]*Research Center for Nuclear Physics (RCNP), Osaka University, Osaka 567-0047, Japan*
[3]*Department of Physics and Astronomy, University of Victoria, Victoria, British Columbia V8W 3P6, Canada*
[4]*Department of Physics, Seoul National University, Seoul 151-742, South Korea*
[5]*National Institute of Physics and Nuclear Engineering - IFIN HH, Bucharest, Romania*
[6]*Stefan-Meyer-Institut für subatomare Physik, A-1020 Vienna, Austria*
[7]*Istituto Nazionale di Fisica Nucleare (INFN), Sezione di Torino, Torino, Italy*
[8]*Dipartimento di Fisica Generale, Universita' di Torino, Torino, Italy*
[9]*Laboratori Nazionali di Frascati dell' INFN, I-00044 Frascati, Italy*
[10]*Department of Physics, Osaka University, Osaka 560-0043, Japan*
[11]*Department of Physics, Kyoto University, Kyoto 606-8502, Japan*
[12]*Department of Physics, The University of Tokyo, Tokyo 113-0033, Japan*
[13]*Laboratory of Physics, Osaka Electro-Communication University, Osaka 572-8530, Japan*
[14]*High Energy Accelerator Research Organization (KEK), Tsukuba 305-0801, Japan*
[15]*Department of Physics, Tokyo Institute of Technology, Tokyo 152-8551, Japan*
[16]*Technische Universität München, D-85748 Garching, Germany*
[17]*Graduate School of Arts and Sciences, The University of Tokyo, Tokyo 153-8902, Japan*
[18]*Department of Physics, Tohoku University, Sendai 980-8578, Japan*
[19]*Korea Institute of Radiological and Medical Sciences (KIRAMS), Seoul 139-706, South Korea*
[20]*ASRC, Japan Atomic Energy Agency, Ibaraki 319-1195, Japan*
[21]*Department of Chemical Physics, Lund University, Lund 221 00, Sweden*
[22]*Research Center for Electron Photon Science (ELPH), Tohoku University, Sendai 982-0826, Japan*
[23]*Engineering Science Laboratory, Chubu University, Aichi 487-8501, Japan*
[24]*Centro Ricerche Fermi-Museo Storico della Fisica e Centro studi e ricerche "Enrico Fermi", 000184 Rome, Italy*

(Received 23 June 2020; accepted 16 September 2020; published 14 October 2020)

We have performed an exclusive measurement of the $K^- + {}^3\mathrm{He} \to \Lambda pn$ reaction at an incident kaon momentum of 1 GeV/c. In the Λp invariant mass spectrum, a clear peak was observed below the mass threshold of $\bar{K}+N+N$, as a signal of the kaonic nuclear bound state, $\bar{K}NN$. The binding energy, decay width, and S-wave Gaussian reaction form factor of this state were observed to be $B_K = 42 \pm 3(\mathrm{stat.})^{+3}_{-4}(\mathrm{syst.})$ MeV, $\Gamma_K = 100 \pm 7(\mathrm{stat.})^{+19}_{-9}(\mathrm{syst.})$ MeV, and $Q_K = 383 \pm 11(\mathrm{stat.})^{+4}_{-1}(\mathrm{syst.})$ MeV/c, respectively. The total production cross section of $\bar{K}NN$, determined by its Λp decay mode, was $\sigma_K^{\mathrm{tot}} BR_{\Lambda p} = 9.3 \pm 0.8(\mathrm{stat.})^{+1.4}_{-1.0}(\mathrm{syst.})$ μb. We estimated the branching ratio of the $\bar{K}NN$ state to the Λp and $\Sigma^0 p$ decay modes as $BR_{\Lambda p}/BR_{\Sigma^0 p} \sim 1.7$, by assuming that the physical processes leading to the ΣNN final states are analogous to those of Λpn.

DOI: 10.1103/PhysRevC.102.044002

*takumi.yamaga@riken.jp
†masa@riken.jp
‡Deceased.

I. INTRODUCTION

The bound system of an antikaon ($\bar{K}$) and a nucleon (N) has been studied ever since the uds-quark resonance, $\Lambda(1405)$, was suggested as a $\bar{K}N$ atomlike state due to the strong $\bar{K}N$ attraction in the isospin zero channel ($I = 0$) by Dalitz *et al.* [1,2]. Based on numerous theoretical calculations of the chiral SU(3) dynamics and lattice quantum chromodynamics (QCD), the interpretation that "$\Lambda(1405)$ has an internal structure of a $\bar{K}N$ atomlike state (mesonic excitation) rather than a quark excited state of a uds baryon" has gained stronger theoretical support [3–5].

Based on $\Lambda(1405)$ being a $\bar{K}N$ atom-like mesonic resonance (or $\bar{K}N$ bound state), the possibility of a more general system containing a $\bar{K}$ in a multinucleon system, called a kaonic nucleus, has also been discussed, in which a molecule-like nuclear state with a specific spatial configuration forms through competing interactions between a strong $\bar{K}N$ ($I = 0$) attraction and short-range NN repulsion. Much theoretical work on these kaonic nuclei, especially in the $\bar{K}NN$ bound state, has been undertaken with various $\bar{K}N$ interaction models and calculation methods [6–21]. The $\bar{K}NN$ bound state has charge $+1$ and isospin $I = 1/2$ (symbolically denoted as K^-pp for the $I_z = +1/2$ state) and its spin and parity are considered to be $J^P = 0^-$. In the framework of the strong interaction, it is a mesonic resonance of a Λp dibaryon system located below the mass threshold of a kaon and two nucleons, having an internal molecule-like structure, N-$\bar{K}$-N, due to the competing interactions. The existence of the $\bar{K}NN$ bound state is generally supported by all the calculations mentioned above; however, the estimated binding energies and widths of the state are widely spread.

To search for the $\bar{K}NN$ bound state, we conducted the experiment J-PARC E15 using the in-flight K^- beam at J-PARC. In the first measurement of the experiment, we demonstrated a significant yield excess well below the $\bar{K}NN$ mass threshold ($M_{\bar{K}NN} = m_{\bar{K}} + 2m_N \sim 2.37$ GeV/c^2) in the inclusive analysis of the ^{3}He(K^-, n) reaction [22], which suggests the strongly attractive nature of the $\bar{K}N$ interaction. We therefore extended the analysis focusing on the simplest exclusive channel, the Λpn final state, which consists of three baryons (YNN) including the lightest hyperon (Y) [23]. Because s-quark conservation is secured in nuclear reactions governed by the strong interaction, we can trace the s-quark flow. Thus, the interaction between a recoiled $\bar{K}$ and two spectator nucleons, $\bar{K}NN$, can be studied by YN-pair analysis, which will tell us the reaction dynamics and formation signature of $\bar{K}NN$, if it exists. As described in Ref. [23], a kinematical anomaly, a concentration of events around $M_{\bar{K}NN}$, was observed only in the Λp invariant mass spectrum. To study this anomaly, we performed a second measurement and found a peak structure in the Λp invariant mass spectrum located below $M_{\bar{K}NN}$, which we interpreted as a signal of the $\bar{K}NN$ bound state [24].

This article is organized as follows. In Sec. II, we give a brief description of the J-PARC E15 experiment and a production process of the $\bar{K}NN$ bound state in the $K^- + {}^3$He reaction. In Sec. III, we introduce event selection criteria for the Λpn final state by detecting Λp and by the kinematical identification of a missing neutron. Then, we present a two-dimensional (2D) distribution of the invariant mass of Λp and the momentum transfer to Λp of the selected events. To distinguish the $\bar{K}NN$ signal from the other reaction processes, we fitted the 2D distribution with three components: K) the $\bar{K}NN$ bound state, F) the nonmesonic quasifree kaon absorption process, and B) a broad distribution covering the whole kinematically allowed region of the Λpn final state. In this way, we clearly isolated the $\bar{K}NN \to \Lambda p$ decay process and obtained the binding energy, decay width, S-wave Gaussian form factor parameter, and production cross section decaying into the Λp mode of the $\bar{K}NN$ bound state, as described in Sec. IV. Finally, we evaluated the effect of the ΣNN final state contamination and estimated the $\bar{K}NN$ decay branch to the $\Sigma^0 p$ channel in a self-consistent way.

II. J-PARC E15 EXPERIMENT

We measured the $K^- + {}^3\mathrm{He} \to \Lambda pn$ reaction to search for the $\bar{K}NN$ bound state by its Λp decay mode. The incident momentum of the K^- beam is chosen to be $p_K = 1$ GeV/c to maximize the cross section of the elementary $K^-N \to \bar{K}N$ reaction, corresponding to $\sqrt{s} = 1.8$ GeV.

Because the kinematical anomaly was found only in the Λp invariant mass of the Λpn final state, we analyzed the process as two successive reactions, i.e.,

$$K^- + {}^3\mathrm{He} \to X + n, \quad X \to \Lambda p. \tag{1}$$

The former two-body reaction can be characterized by two parameters, the invariant mass of X (m_X) and momentum transfer to X (q_X). In a more microscopic way, the X formation reaction described in the framework of the cascade reactions can be

$$K^- + N \to \bar{K} + n, \quad \bar{K} + NN \to X, \tag{2}$$

in which a virtual kaon $\bar{K}$ is produced in the primary reaction between a K^- and a nucleon followed by a formation reaction of the X resonance together with two spectator nucleons.

In these reactions, m_X corresponds to the invariant mass of the $\bar{K} + NN$ system, and q_X is the three-momentum of the intermediate virtual $\bar{K}$ that can be measured by the momentum of $\Lambda + p$ in the final state in the laboratory frame. At $p_K = 1$ GeV/c, the minimum q_X is as small as $\sim$200 MeV/c when the neutron is formed in the forward direction, so we can expect a large $\bar{K}$ sticking probability to the two residual nucleons.

The experiment was performed at the hadron experimental facility of J-PARC. A high-intensity secondary K^- beam, produced by bombarding a primary gold target with a 30-GeV proton beam, is transported along the K1.8BR beam line. Other secondary particles in the beam are removed by an electrostatic separator.

A beam-line detector system and a cylindrical detector system (CDS) are used to measure incident K^- and scattered charged particles, respectively. A detailed description of the experimental setup is given in Refs. [25–27]; however, we summarize the basics as follows.

The beam-line detector system measures the time of flight and momentum of the K^- beam. At the on-line level, K^-

is identified by an aerogel Cherenkov detector. The position and direction of the beam are measured by a drift chamber located just in front of the experimental target of liquid ^{3}He. The liquid ^{3}He target is located at the final focus point of the beam line. The target cell of ^{3}He has a cylindrical shape with a diameter of 68 mm and a length along the beam direction of 137 mm, and has a density of $\sim$80 mg/cm^3. We accumulated ^{3}He-filled data as the experimental run, and the empty target data as a background study. The CDS surrounding the ^{3}He target is composed of a cylindrical drift chamber and a cylindrical hodoscope. The detectors are installed inside a solenoid magnet to measure the momenta of the scattered charged particles.

III. ANALYSIS

Particle identification and momentum reconstruction of the K^- beam and scattered charged particles were performed. Then, the $K^- + {}^3\mathrm{He} \to \Lambda pn$ final state was selected, where Λ and p were detected by CDS and the missing-n was identified kinematically. For the selected Λpn events, we measured a 2D distribution of the invariant mass of the Λp and the momentum transfer to the Λp. To investigate the production of the $\bar{K}NN$ bound state, we conducted a spectral fitting to the 2D distribution.

A. Beam and scattered particle analysis

For the K^- beam, we applied time-of-flight-based PID selection to achieve a high purity of kaon identification. Contamination from the in-flight kaon decay was rejected by checking the track inconsistency as a particle trajectory recorded by drift chambers. The beam momentum was determined with a second-order transfer matrix of the final beam-line dipole spectrometer magnet calculated using the TRANSPORT code [28]. A typical momentum resolution was estimated to be 0.2%.

The trajectories of the charged particles from the $K^- + {}^3\mathrm{He}$ reaction were measured by the CDS. We designed the magnet to have sufficient magnetic uniformity in the effective region of the CDS to apply a simple helical fit to each trajectory to analyze its momentum. The absolute magnetic field strength was 0.715 T, calibrated using monochromatic invariant-mass peaks of $K^0_s \to \pi^+\pi^-$ and $\Lambda \to p\pi^-$ decays. The PID was conducted by a conventional method based on the 2D event distribution over the mass-square and momentum. In the present analysis, a $\pm 2.5\,\sigma$ region from the intrinsic mass was selected for each particle. Any overlap of two different PID regions was rejected to reduce miss-identification [23]. The inefficiency due to the overlap rejection was corrected in the analysis. After the particle identification, an energy-loss correction was applied by considering all the materials on the trajectory of the particle to obtain its initial momentum.

B. Event selection of Λpn final state

To select the $K^- + {}^3\mathrm{He} \to \Lambda pn$ reaction, three charged particles, $pp\pi^-$, were required. From the $pp\pi^-$, we examined two possible $p\pi^-$ pairs as for Λ candidates (Λ'). A candidate trajectory is tentatively defined by the $p\pi^-$ vertex (the nearest point of the two trajectories) and synthetic momentum vector of the two. Then, we checked if the event kinematics is consistent with the Λpn final state, by a kinematical fitting. In the kinematical fitting, the $p\pi^-$-pair invariant mass ($m_{p\pi^-}$) and the $pp\pi^-$ missing mass (m_{R^0} in the $^3\mathrm{He}(K^-, pp\pi^-)R^0$ reaction) are used to derive the χ^2 (degrees of freedom =2, in the present case) as an indicator of the kinematical consistency to be the Λpn final state. The KinFitter package based on the ROOT classes [29] was used to search for the minimum χ^2.

To include geometrical consistency of the event topology in the consistency test, a log-likelihood $l(\boldsymbol{x})$ is introduced as

$$l(\boldsymbol{x}) = -\ln \prod_{i=1}^{5} p_i(x_i), \tag{3}$$

where p_i is the probability density function of the ith variable estimated by a Monte Carlo simulation, and the maximum value is renormalized to be one, so as to make $l(\boldsymbol{x}) = 0$ at the most probable density point of the parameter set. $\boldsymbol{x}$ stands for

$$\boldsymbol{x} = (\chi^2, D_{K^-p}, D_{K^-\Lambda'}, D_{\Lambda' p}, D_{p\pi^-}), \tag{4}$$

where the five variables are the χ^2 given by the kinematical fitting, the distances of closest approach for incoming K^- with p (D_{K^-p}) and with Λ' ($D_{K^-\Lambda'}$), the distance of closest approach of Λ' and p ($D_{\Lambda' p}$), and the minimum approach of the $p\pi^-$ pair at the Λ' decay point ($D_{p\pi^-}$). Finally, both the $K^-\Lambda'$ and K^-p vertices were required to be in the fiducial volume of the target, to reduce the background from the target cell. In this examination, more than 99.5% of the $p\pi^-$ were paired correctly in the simulation.

The event distribution of m_{R^0} and $l(\boldsymbol{x})$ is shown as a 2D plot in Fig. 1(a). A strong event concentration is seen at the bottom of the figure, which corresponds to the nonmesonic Λpn final state. As shown in the m_{R^0} spectrum, Fig. 1(b), Λpn events make a clear peak at m_n, and the events are clearly separated from the mesonic ($YNN + \pi$) final states located at $m_{R^0} > m_N + m_\pi$. To improve the Λpn-selection, we selected Λpn events on the 2D plane of m_{R^0} and $l(\boldsymbol{x})$, as indicated by the red line in Fig. 1(a).

The 2D plot of $m_{p\pi^-}$ and $l(\boldsymbol{x})$, applying the Λpn-selection window, is shown in Fig. 2(a), and the projection onto $m_{p\pi^-}$ is shown in Fig. 2(b). As shown in the figure, Λ is clearly selected. The tail of the Λ peak is quite small; however, we should note that it does not secure the purity of the Λpn final state, in that the tail is removed by the kinematical fitting procedure through the χ^2 evaluation. In the present Λpn selection, the other final states may come in, as is indicated in Fig. 1(a).

To evaluate the contamination yields of the other final states, we conducted a detailed simulation as shown in Fig. 3. In this simulation, we generated nonmesonic YNN final states (Λpn, $\Sigma^0 pn$, and $\Sigma^- pp$) according to the fit result (described in Sec. IV A) to make the simulation realistic. For simplicity, the event distribution of mesonic final states, which make smaller contributions to the Λpn-selection window, are generated proportional to the phase space.

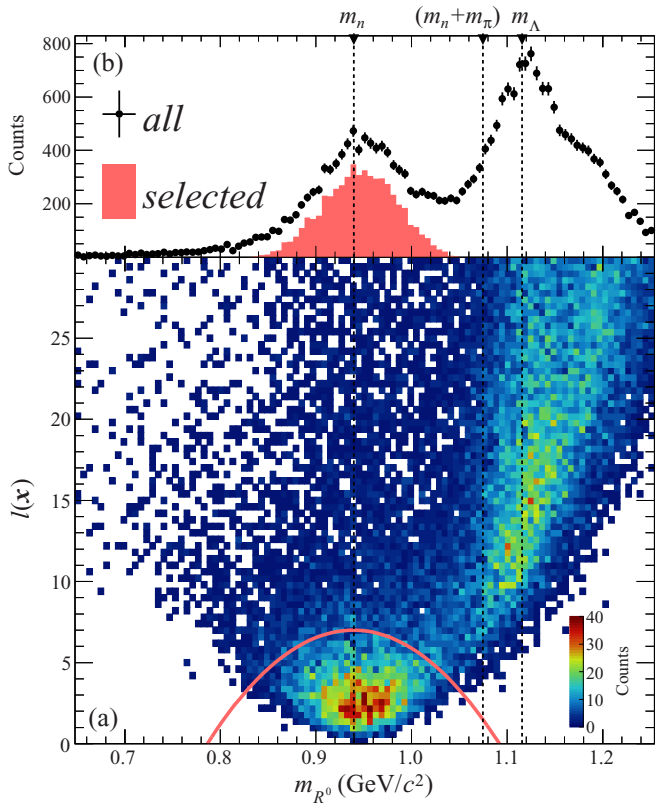

FIG. 1. (a) 2D plot of m_{R^0} and $l(\boldsymbol{x})$, where m_{R^0} is the missing mass of the ^{3}He$(K^-, pp\pi^-)R^0$ reaction and $l(\boldsymbol{x})$ is the event consistency with Λpn. (b) Projected spectrum of the m_{R^0} axis by selecting $l(\boldsymbol{x}) < 30$. The vertical black dashed lines are the masses of n (m_n), $N + \pi^0$ ($m_N + m_\pi$), and Λ (m_Λ). The Λpn event was selected below the red line in the 2D plot. The projection of selected events is shown by the red histogram in (b).

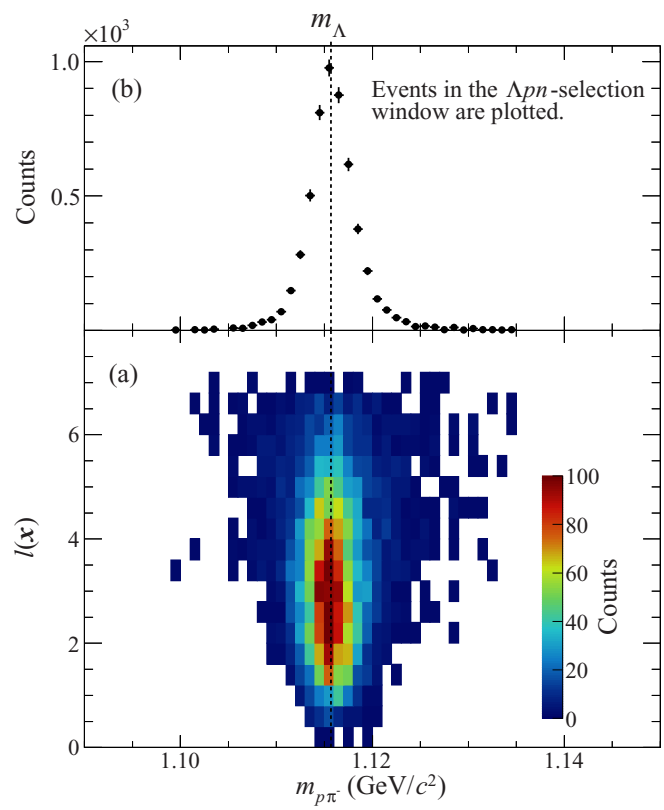

FIG. 2. (a) 2D plot of $m_{p\pi^-}$ and $l(\boldsymbol{x})$. (b) Projected spectrum on the $m_{p\pi^-}$ axis. Events in the Λpn-selection window [shown in Fig. 1(a)] are plotted. The vertical black dashed line is the Λ mass.

As shown in Fig. 3(a), it is difficult to eliminate the $\Sigma^0 pn$ and $\Sigma^- pp$ final state events in the Λpn-selection window, since the m_{R^0} spectra of contaminations of the two components are very similar. In particular, the Λpn and $\Sigma^- pp$ final states have the same m_{R^0} distribution. This is because $R^0 = n$, $\gamma + n$, and n for the Λpn, $\Sigma^0 pn$, and $\Sigma^- pp$ final states, respectively. Thus, we plotted the m_{R^-} spectrum of ^{3}He$(K^-, pp)R^-$, as shown in Fig. 3(b), to give $R^- = \pi^- + n$, $\pi^- + \gamma + n$, and Σ^- for the Λpn, $\Sigma^0 pn$, and $\Sigma^- pp$ final states, respectively. As shown in the figure, the relative yields can be evaluated easily, since the $\Sigma^- pp$ final state makes a peak at the Σ^- intrinsic mass, while the Λpn final state becomes even broader in the m_{R^-} distribution. Figure 3(c) is the projection of the events onto $l(\boldsymbol{x})$, where the Λpn final state has smaller $l(\boldsymbol{x})$ than the other final states.

The relative yields of the signal and contaminations in the present Λpn-selection window were estimated by the simultaneous fitting of these three spectra. The result is summarized in Table I. The fitting results were improved substantially by applying a realistic Λpn distribution, together with the $\Sigma^0 pn$ and $\Sigma^- pp$ contributions to the spectra. However, the fitting results, with a χ-square of 917 over 506 degrees of freedom, shown in Fig. 3, might not be sufficient. This is because we accepted events having a relatively large $l(\boldsymbol{x})$ in evaluating the contamination from the mesonic final states, whose distribution is simply assumed to be proportional to the phase space. Thus, the systematic uncertainties of the table were evaluated by limiting the fitting data region of Fig. 3 to $l(\boldsymbol{x}) < 10$ to reduce the contamination effect from mesonic final states.

Contaminations from the mesonic final state and from the K^- reaction at the target cell are negligible. Thus, we focused on the nonmesonic $\Sigma^0 pn$ and $\Sigma^- pp$ final states (ΣNN) in the following analysis (Sec. III E).

C. m_X and q_X distributions

For the Λpn-selected events, we measured the invariant mass of the Λp system (m_X) and the momentum transfer to the Λp system (q_X). As shown in Eq. (1), q_X can be given by the momenta of Λ ($\boldsymbol{p}_\Lambda$) and p ($\boldsymbol{p}_p$) as

$$q_X = |\boldsymbol{p}_\Lambda + \boldsymbol{p}_p|. \tag{5}$$

Figure 4 shows the 2D event distribution on the m_X and q_X plane. As shown in the figure, there are very strong event-concentrating regions. To show these event concentrations in an unbiased manner, an acceptance correction was applied to the data, to make the results independent of both the experimental setup and analysis code. The events density, represented by a color code, is given in units of the double

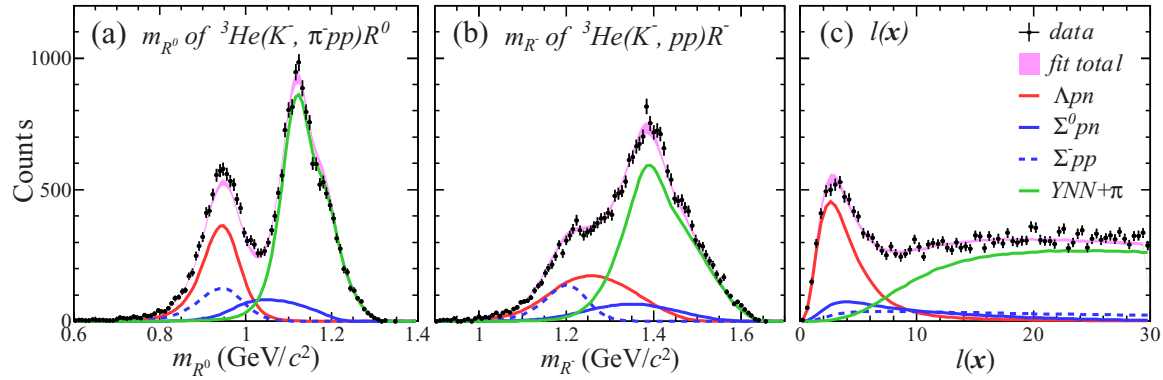

FIG. 3. Distributions of (a) m_{R^0} of $^3\mathrm{He}(K^-, \pi^- pp)R^0$ [the same as Fig. 1(b)], (b) m_{R^-} of $^3\mathrm{He}(K^-, pp)R^-$, and (c) $l(\boldsymbol{x})$. For the m_{R^0} and m_{R^-} spectra, $l(\boldsymbol{x}) < 30$ was selected. These three distributions were simultaneously fitted by simulated spectra shown by colored lines. The fitting χ-square and number of degrees of freedom were 917 and 506, respectively. For mesonic ($YNN + \pi$), the final states all of possible charged states and combinations were summed.

differential cross section:

$$\frac{d^2\sigma}{dm_X\, dq_X} = \frac{N(m_X, q_X)}{\varepsilon(m_X, q_X)} \frac{1}{\Delta m_X} \frac{1}{\Delta q_X} \frac{1}{\mathcal{L}}, \tag{6}$$

where $N(m_X, q_X)$ is the obtained event number in $\Delta m_X = 10\ \mathrm{MeV}/c^2$ and $\Delta q_X = 20\ \mathrm{MeV}/c$ (bin widths of m_X and q_X, respectively). $\mathcal{L}$ is the integrated luminosity, evaluated to be $2.89 \pm 0.01\ \mathrm{nb}^{-1}$. $\varepsilon(m_X, q_X)$ is the experimental efficiency, which is quite smooth, as shown in Fig. 5(a), around all the events-concentrating regions of Fig. 4.

After the acceptance correction, if no intermediate state, such as X, exists in the $K^- + {}^3\mathrm{He} \to \Lambda pn$ reaction, then the event distribution will simply follow the Λpn phase space $\rho(m_X, q_X)$ without having a specific form factor, as given in Fig. 5(b). However, $\rho(m_X, q_X)$ is smooth for the entire kinematically allowed region, in contrast to the data in Fig. 4.

To account for the observed event distribution, three physical processes were introduced, as in Ref. [24]. Details of the physical processes, the formulation of each fitting function, and the fitting procedures are described in the following sections.

D. 2D model fitting functions

We considered the following three processes: K) the $\bar{K}NN$ bound state, F) the nonmesonic quasifree (QF) kaon absorption ($\mathrm{QF}_{\bar{K}-\mathrm{abs}}$) process, and B) a broad distribution covering the whole kinematically allowed region of the Λpn final state.

TABLE I. Relative yields of signal and contaminations in the present Λpn selection. The first and second errors are statistical and systematic, respectively.

Source	Relative yield (R_j) (%)
Λpn (signal)	$76.3 \pm 1.6 \pm 0.5$
$\Sigma^0 pn$	$12.0 \pm 0.8 \pm 0.6$
$\Sigma^- pp$	$7.1 \pm 0.3 \pm 1.4$
Total mesonic final states	$1.5 \pm 0.1 \pm 0.4$
K^- reaction at the target cell	$3.1 \pm 0.0 \pm 0.4$

To decompose those processes, we conducted 2D fitting for the event distribution.

The production yields of these three processes [$F_i(m_X, q_X)$ for $i = K, F, B$] observed in the Λpn final state should be proportional to the Λpn phase space $\rho(m_X, q_X)$. Thus, $F_i(m_X, q_X)$ can be described as the product of $\rho(m_X, q_X)$ and specific spectral terms for the ith process of a component $f_i(m_X, q_X)$, as

$$F_i(m_X, q_X) = \rho(m_X, q_X) f_i(m_X, q_X). \tag{7}$$

Figure 6 shows typical 2D distributions of $f_i(m_X, q_X)$ for the three processes. All the parameters of the fitting functions described below are fixed to the final fitting values.

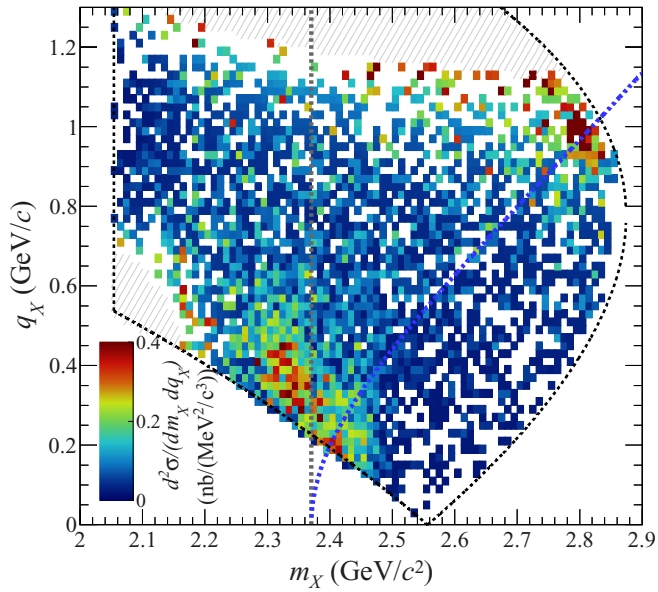

FIG. 4. 2D plot on the m_X and q_X plane after acceptance correction. The black dotted line shows the kinematical limit of the reaction. The vertical gray dotted line and blue dotted curve are $M_{\bar{K}NN}$ and $M_F(q)$, respectively. The gray hatched regions indicate where the experimental efficiency is <0.5%.

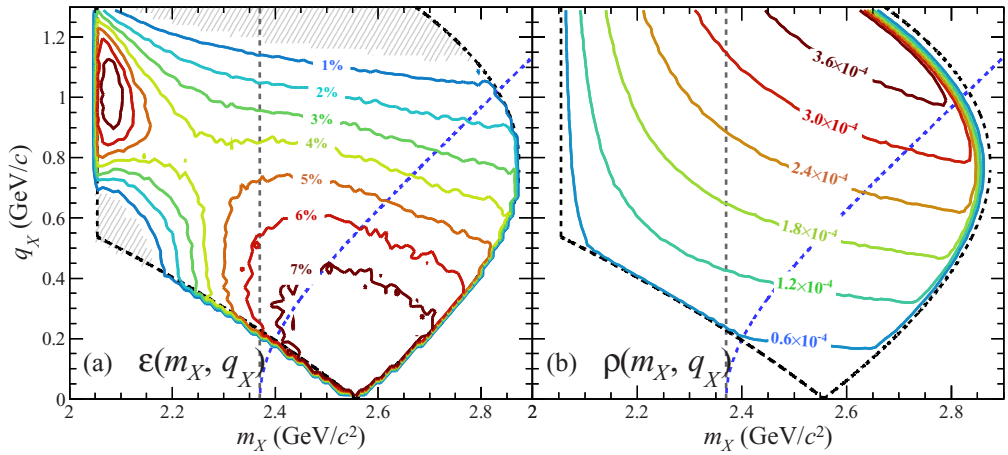

FIG. 5. (a) Simulated spectra of experimental efficiency $\varepsilon(m_X, q_X)$ for Λpn final states. $\varepsilon(m_X, q_X)$ includes geometrical acceptance of CDS and analysis efficiency (decay branching ratio of Λ is also taken into account). The efficiency is calculated bin by bin. The hatched regions are insensitive in the present setup, where $\varepsilon < 0.5\%$. (b) Lorentz-invariant Λpn phase space $\rho(m_X, q_X)$ taking into account the kaon beam momentum bite. The ratio is normalized by one generated event. The roughness of the contours in both (a) and (b) is due to the limited statistics of the simulation. The vertical gray dotted lines and blue dotted curves are the same as in Fig. 4.

To make f_i automatically fulfill time-reversal symmetry, we limited ourselves to using q_X-even terms to formulate the fitting functions described below, with one exception. The details and the reason for the exception are described below.

1. $\bar{K}NN$ production ($i = K$)

As described in Ref. [24], we formulated the formation cross section of the $\bar{K}NN$ bound state according to the reaction in Eq. (1) with a plane-wave impulse approximation (PWIA) with a harmonic oscillator wave function. In this way, we simplified the microscopic reaction mechanism in Eq. (2). The time integral gives a Breit-Wigner formula in the m_X direction, and the spatial-integral gives a S-wave Gaussian form factor as

$$f_K(m_X, q_X) = \frac{(\Gamma_K/2)^2}{(m_X - M_K)^2 + (\Gamma_K/2)^2} \times A_0^K \exp\left(-\frac{q_X^2}{Q_K^2}\right), \tag{8}$$

where M_K, Γ_K, and Q_K are the mass, decay width, and reaction form factor (involving microscopic reaction dynamics) parameter for the bound state, respectively. In the formula, we assumed that the spatial size of the bound state is much smaller than that of ^{3}He, so the size term of ^{3}He was ignored.

2. Nonmesonic $\mathrm{QF}_{\bar{K}-\mathrm{abs}}$ process ($i = F$)

When the invariant mass m_X of the secondary reaction in Eq. (2) is larger than the threshold $M_{\bar{K}NN}$, the recoil-kaon can

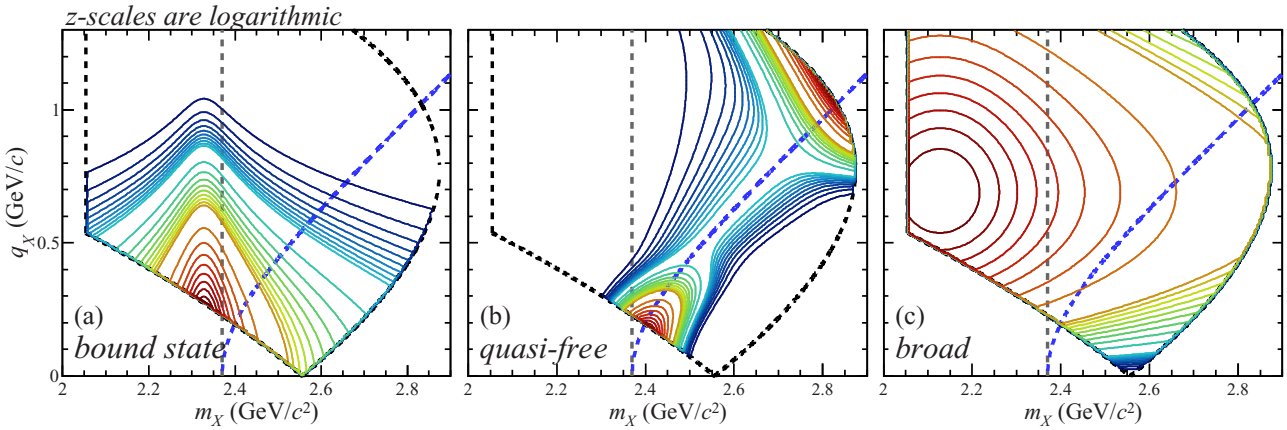

FIG. 6. 2D spectral functions for (a) the $\bar{K}NN$ bound state $f_K(m_X, q_X)$ [see Eq. (8)], (b) the $\mathrm{QF}_{\bar{K}-\mathrm{abs}}$ process $f_F(m_X, q_X)$ [see Eq. (10)], and (c) a broad distribution $f_B(m_X, q_X)$ [see Eq. (12)]. For all the figures, the function strength is given in a logarithmic scale, where the contours are in the steps of 10% (red–orange), 1% (orange–cyan), and 0.1% (cyan–blue) compared to the maximum density of each function. The vertical gray dotted lines and blue dotted curves are the same as in Fig. 4.

behave as an ≈ free particle (on-mass shell), and that quasifree kaon may be absorbed by spectator nucleons. Thus, X can be any channel, such as $\bar{K}+N+N$, $Y+N$, or other mesonic channels, if $m_X > M_{\bar{K}NN}$. Among these, we denote the $Y+N$ channel as the nonmesonic $\mathrm{QF}_{\bar{K}-\mathrm{abs}}$ process. Specifically, Y and N are Λ and p in the Λpn final state. In the nonmesonic $\mathrm{QF}_{\bar{K}-\mathrm{abs}}$ process, a recoiled $\bar{K}$ is almost on-shell and absorbed by the two spectator nucleons. In $\mathrm{QF}_{\bar{K}-\mathrm{abs}}$, q_X is predominantly defined by the neutron emission angle, because the residual nucleons are spectators (almost at-rest). Thus, the m_X distribution-centroid is kinematically given as

$$M_F(q_X) = \sqrt{4m_N^2 + m_{\bar{K}}^2 + 4m_N\sqrt{m_{\bar{K}}^2 + q_X^2}}, \tag{9}$$

where m_N and $m_{\bar{K}}$ are the intrinsic mass of N and $\bar{K}$, respectively. We plotted the $M_F(q_X)$ curve in Fig. 4 as a blue dotted line. In the figure, two event concentrations on $M_F(q_X)$ are clearly seen around $q_X \sim 0.2$ GeV/c and ∼1.0 GeV/c. These event concentrations correspond to the backward and forward scattered $\bar{K}$ in the elementary $K^-N \to \bar{K}n$ reaction. The $\mathrm{QF}_{\bar{K}-\mathrm{abs}}$ should distribute around $M_F(q_X)$ in the m_X direction due to the Fermi motion of the two nucleons. To describe the distribution, a Gaussian function is utilized, as

$$f_F(m_X, q_X) = \exp\left[-\frac{(m_X - M_F(q_X))^2}{\sigma^2(q_X)}\right] \times \left[A_0^F \exp\left(-\frac{q_X^2}{Q_F^2}\right) + A_1^F + A_2^F \exp\left(\frac{m_X}{m_0} + \frac{q_X}{q_0}\right)\right]. \tag{10}$$

In the formula, we allowed the m_X distribution width to have a q_X dependence as

$$\sigma(q_X) = \sigma_0 + \sigma_2 q_X^2. \tag{11}$$

The second angle bracket in Eq. (10) represents the q_X dependence of the production yield of the $\mathrm{QF}_{\bar{K}-\mathrm{abs}}$ process, while the middle term defines a flat distribution, and the first and third terms correspond to backward and forward scattered $\bar{K}$ events, respectively.

The forward $\bar{K}$ part of the $\mathrm{QF}_{\bar{K}-\mathrm{abs}}$ process is located far from the region of interest (distributed around the projectile K^- momentum ∼ 1 GeV/c), as shown in Figs. 4 and 6(b), so we phenomenologically formulated our model fitting function as a simple exponential (not as q_X even), as given in Eq. (10).

3. Broad distribution ($i = B$)

The two reaction processes described above have specific regions where events concentrate. However, there is a broad distribution over the entire kinematically allowed region in (m_X, q_X). In contrast to other processes, Λ, p, and n share the kinetic energy rather randomly, resulting in a relatively weak m_X and q_X dependence, similar to a pointlike interaction whose cross section should be proportional to $\rho(m_X, q_X)$, and thus $f_i(m_X, q_X) \sim$ constant. Therefore, a natural interpretation of this component is the three-nucleon absorption (3NA) reaction of an incident K^-. On the other hand, there is a weak but yet clear m_X and q_X dependence over the whole kinematical region. The event density at higher m_X and lower q_X is much weaker than that at the opposite side. On the other hand, there is no clear event density correlation between m_X and q_X, which indicates that the distribution could be described by the Cartesian product of centroid concentrating functions in both m_X and q_X. The most natural formula can be written as an extension of Eq. (8) as

$$f_B(m_X, q_X) = \frac{(\Gamma_B/2)^2}{(m_X - M_B)^2 + (\Gamma_B/2)^2} \times \left(A_0^B + A_2^B \frac{q_X^2}{Q_B^2}\right) \exp\left(-\frac{q_X^2}{Q_B^2}\right). \tag{12}$$

4. m_X spectra of Λpn final state

To demonstrate the applicability of the model fitting functions conceptually, we present the m_X spectrum of the data in the Λpn-selection window and compare it with the m_X spectral shapes, restricting ourselves to the Λpn final state (excluding ΣNN), for K) $\bar{K}NN$, F) $\mathrm{QF}_{\bar{K}-\mathrm{abs}}$, and B) the broad distribution, as shown in Fig. 7. For comparison, the acceptance was corrected for the data Fig. 7(a) by dividing the data by $\varepsilon(m_X, q_X)$ bin by bin [except for $\varepsilon(m_X, q_X) < 0.5\%$]. For the same reason, weighting of the phase-space volume was applied to Fig. 7(b) by multiplying each function by $\rho(m_X, q_X)$. Both figures were integrated over the whole q_X region. All the parameters of the fitting functions of Fig. 7(b) were fixed to the final fitting value. For the figure, the 2D experimental resolution (depending on both m_X and q_X) was considered in the Monte Carlo simulation. The magenta band is the sum of all the reaction components and the band width indicates the fit error.

As shown in the figure, the global structure of the m_X spectrum is qualitatively described only with the Λpn final state, even before considering the ΣNN contribution, as expected. The quantitative fitting was performed by considering ΣNN effects, as described in the following section.

E. Effect of ΣNN contamination

As we described in Sec. III B, the selected Λpn events are not free from the ΣNN ($\Sigma^0 pn$ and $\Sigma^- pp$) final state contaminations.

It is clear that an ideal method to evaluate the contaminations is to observe the ΣNN final state separately. Unfortunately, this is not possible with the present experimental setup. In the present analysis, we assumed the ΣNN channels are produced in analog reaction processes with that of Λpn, i.e., K) $\bar{K}NN$, F) $\mathrm{QF}_{\bar{K}-\mathrm{abs}}$, and B) the broad distribution, and thus the same functions f_i as the Λpn final state can be applied to represent the (m_X, q_X) event distribution of the ΣNN final states. When f_i and its parameters are given as a common function, the YNN final states and their contributions to the spectra through the Λpn-selection window can be reliably evaluated by expanding F_i to F_i^j so the formula is also applicable to ΣNN, where $j = (\Lambda pn, \Sigma^0 pn, \Sigma^- pp)$ and $F_i^j = \rho_j f_i$. ρ and ε can also be expanded to account for each final state in the same manner.

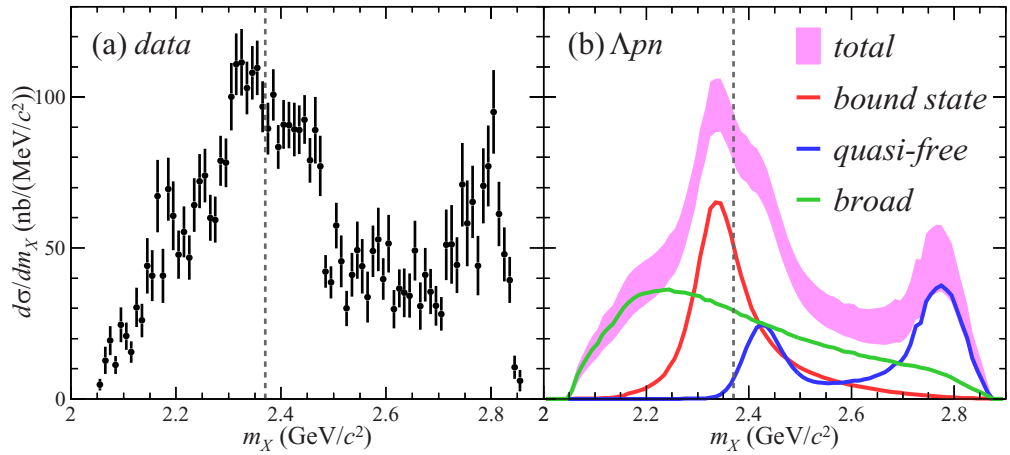

FIG. 7. m_X distribution (integrated by q_X over the whole kinematically allowed region) of (a) data and (b) model functions. The model function is limited to the Λpn final state; i.e., the ΣNN contribution is excluded. The colored lines are spectra of three processes. The magenta thick curve is the sum of all the processes with an error band of the 95% confidence level. The vertical gray dotted lines are $M_{\bar{K}NN}$.

For the $\Sigma^0 pn$ final state, X is produced in the same way as the Λpn final state, but X goes to $\Sigma^0 p$ instead of Λp. Because Σ^0 decays to $\gamma\Lambda$ (100%), part of the $\Sigma^0 pn$ final state leaks in the Λpn-selection window. As shown in Fig. 8(a), the simulated acceptance over $(m_{\Sigma^0 p}, q_{\Sigma^0 p})$ is smaller but similar to Fig. 5(b). The expected m_X and q_X for the contaminating events are also simulated, and the resulting m_X spectrum is shown in Fig. 9(a). As shown in the figure, the structure in the spectrum is similar but shifted to the lower side compared to Fig. 7(b), due to the missing energy of the γ ray.

In contrast, the situation is very different for the $\Sigma^- pp$ final state. We simulated this channel in the same manner to that used for the $\Sigma^0 pn$ final state by replacing a $\Sigma^0 p$ pair with a $\Sigma^- p$ pair. The Σ^- decays to $n\pi^-$ ($\sim$100%). When the invariant mass of the π^- and one of the protons in this final state happen to be close to the Λ intrinsic mass, the event may enter the Λpn-selection window. This makes the simulated acceptance over $(m_{\Sigma^- p}, q_{\Sigma^- p})$ very different from the other two, as given in Fig. 8(b).

We simulated m_X and q_X of the contaminated events for the incorrect Λp pair (pseudo-Λp pair), which would be analyzed as the Λpn final state in the analysis code. The resulting m_X spectrum is given in Fig. 9(b). As shown in the figure, the structure in the spectrum is also totally different from the other m_X spectra. It should be noted that we generated the $I_z = -1/2$ $\bar{K}NN$ ($\bar{K}^0 nn$) bound state instead of $I_z = +1/2$ in this $\Sigma^- pp$ simulation at the same relative yield with the other two final states. This assumption might not be valid, because the isospin combination in the formation channel is different. However, it does not affect the fitting, because events from $\bar{K}NN$ concentrate at the lower q_X side, as shown in Fig. 6(a), where our detector system does not have sensitivity for the $\Sigma^- pp$ final state, as shown by the hatched region in Fig. 8(b). For the same reason, the contribution from the $\mathrm{QF}_{\bar{K}-\mathrm{abs}}$

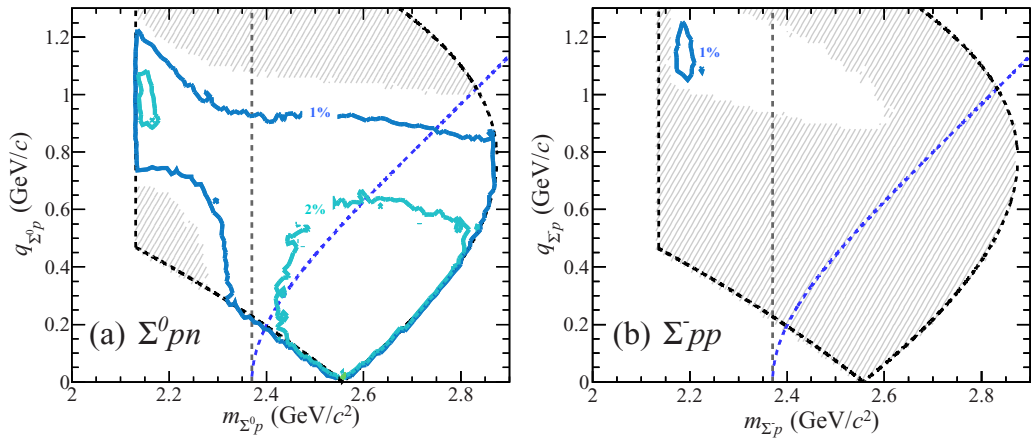

FIG. 8. Experimental acceptance for each ΣNN contamination: (a) $\Sigma^0 pn$ final state and (b) $\Sigma^- pp$ final state. The vertical and horizontal axes for $\Sigma^0 pn$ ($\Sigma^- pp$) are the momentum transfer and invariant mass of the $\Sigma^0 p$ ($\Sigma^- p$) system. The hatched regions are insensitive in the present setup, where $\varepsilon < 0.5\%$. The roughness of the contours is due to the limited statistics of the simulation. The efficiency is calculated bin by bin. The vertical gray dotted lines and blue dotted curves are the same as in Fig. 4.

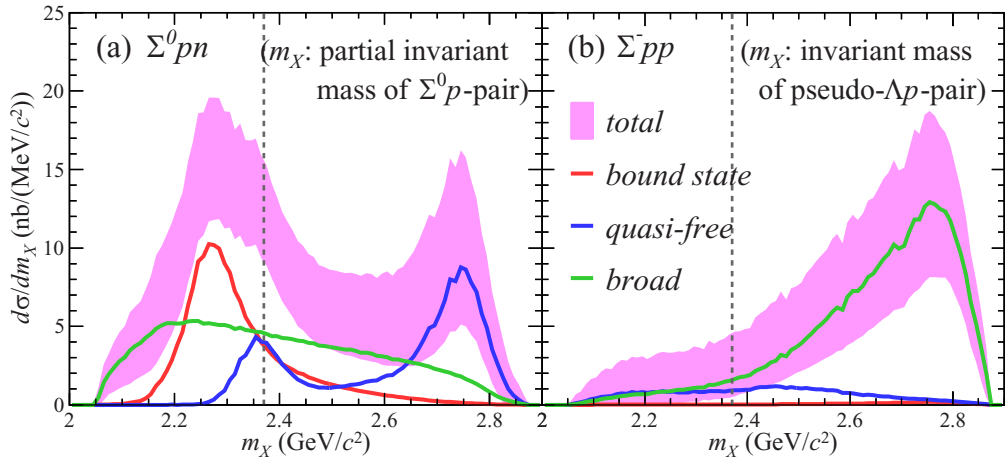

FIG. 9. Expected spectral shapes of m_X for the (a) $\Sigma^0 pn$ final state and (b) $\Sigma^- pp$ final state. The horizontal axis of (a) is the Λp invariant mass, which is a partial invariant mass of $\Sigma^0 p$, where γ of $\Sigma^0 \to \gamma\Lambda$ is missing. The axis of (b) is the Λp invariant mass after misidentification as the Λpn final state; i.e., X is a pair of pseudo-Λ and p. The vertical gray dotted lines are $M_{\bar{K}NN}$. Note that the full scale of the differential cross section is different from that of Fig. 7.

process to this final state is much smaller than those in the other final states.

F. Iterative fitting procedure

To determine the spectroscopic parameters, we conducted 2D fitting for the 2D event distribution, as described in Ref. [24]. As shown in Fig. 5(a) by the gray hatching, the present setup has insensitive regions due to the geometrical coverage of the CDS. To avoid spurious bias caused by the acceptance correction, we directly compared the data and the fitting function in the count base by computing the expected event numbers $\lambda(m_X, q_X)$ to be observed in a (m_X, q_X) bin by

$$\begin{aligned}\lambda(m_X, q_X) &= \sum_{i,j} R_j\, \varepsilon_j(m_X, q_X)\, F_i^j(m_X, q_X)\, \Delta m_X\, \Delta q_X \\ &= \sum_{i,j} R_j\, \varepsilon_j(m_X, q_X)\, \rho_j(m_X, q_X)\, f_i(m_X, q_X) \\ &\quad \times \Delta m_X\, \Delta q_X, \end{aligned} \tag{13}$$

where Δm_X and Δq_X are the bin widths. Then, we evaluated the probability of observing data in the (m_X, q_X) bin as $P(Z = N(m_X, q_X))$, where P is the Poisson distribution function, $N(m_X, q_X)$ is the data counts at the (m_X, q_X) bin, and Z is a random Poisson variable for the expectation value of $\lambda(m_X, q_X)$. The log-likelihood for the 2D fitting $\ln L$ can be defined as an ensemble of probabilities as

$$\ln L = -\sum_{m_X, q_X} \ln(P(Z = N(m_X, q_X))), \tag{14}$$

and the maximum $\ln L$ was obtained to fit the data by optimizing the spectroscopic parameters. There are a total of 17 parameters in this fitting, consisting of four parameters for the $\bar{K}NN$ bound state, eight parameters for the nonmesonic $\mathrm{QF}_{\bar{K}-\mathrm{abs}}$ process, and five parameters for the broad component. For the summation for $\ln L$, we omitted the (m_X, q_X) bin having no statistical significance where $\varepsilon_j(m_X, q_X) < 0.5\%$.

It is very important to apply the acceptance correction to properly represent the physics behind the system. It is also true that the spectra cannot be presented in the scale of the cross-section. Therefore, we applied acceptance correction for the events in the Λpn-selection window after the fitting procedure converged by dividing the spectra by $\varepsilon_{\Lambda pn}(m_X, q_X)$ bin by bin for both the data and fit results, except for Figs. 1–3.

Because the $\bar{K}NN$ signal is concentrated at a specific (m_X, q_X) region, as shown in Fig. 4, we applied the following procedure for the 2D fit. We performed a first fitting for the whole region as the global fit, then performed a second fitting for only the q_X region from 0.3 to 0.6 GeV/c to focus on $\bar{K}NN$. The second fitting was conducted to deduce the parameters of $\bar{K}NN$ under a better S/N region, so the other parameters are fixed in the second fitting. After an iteration of a spectral fitting for the data shown in Fig. 4, we looped back to evaluate the ratio of the final state yields of $\Lambda pn : \Sigma^0 pn : \Sigma^- pp :$ *other* in the Λpn-selection window by the fitting procedure described in Sec. III B (see Fig. 3 and Table I). To obtain self-consistent results, we looped back over the two procedures iteratively until both the ratio parameters and spectroscopic parameters converge.

IV. RESULTS AND DISCUSSION

A. 2D fitted spectra

To demonstrate the accuracy of the fit result in 2D, we plotted the fit result for the m_X spectra in the q_X slice (as shown in Fig. 10) and for the q_X spectra in the m_X-slice (as shown in Fig. 11), i.e., projections of 2D data onto the m_X axis and q_X axis at the same time. In other words, Figs. 10 and 11 show the compilation of event projections of the two-dimensional four-by-four m_X and q_X regions of Fig. 4 onto each axis. In each spectrum, data are compared with the fit result as shown in the magenta band (95% confidence level), and decomposed as colored lines. All the regions are well reproduced for both the m_X and q_X spectra. The maximum log-likelihood and total number of degrees of freedom for the fitting process were

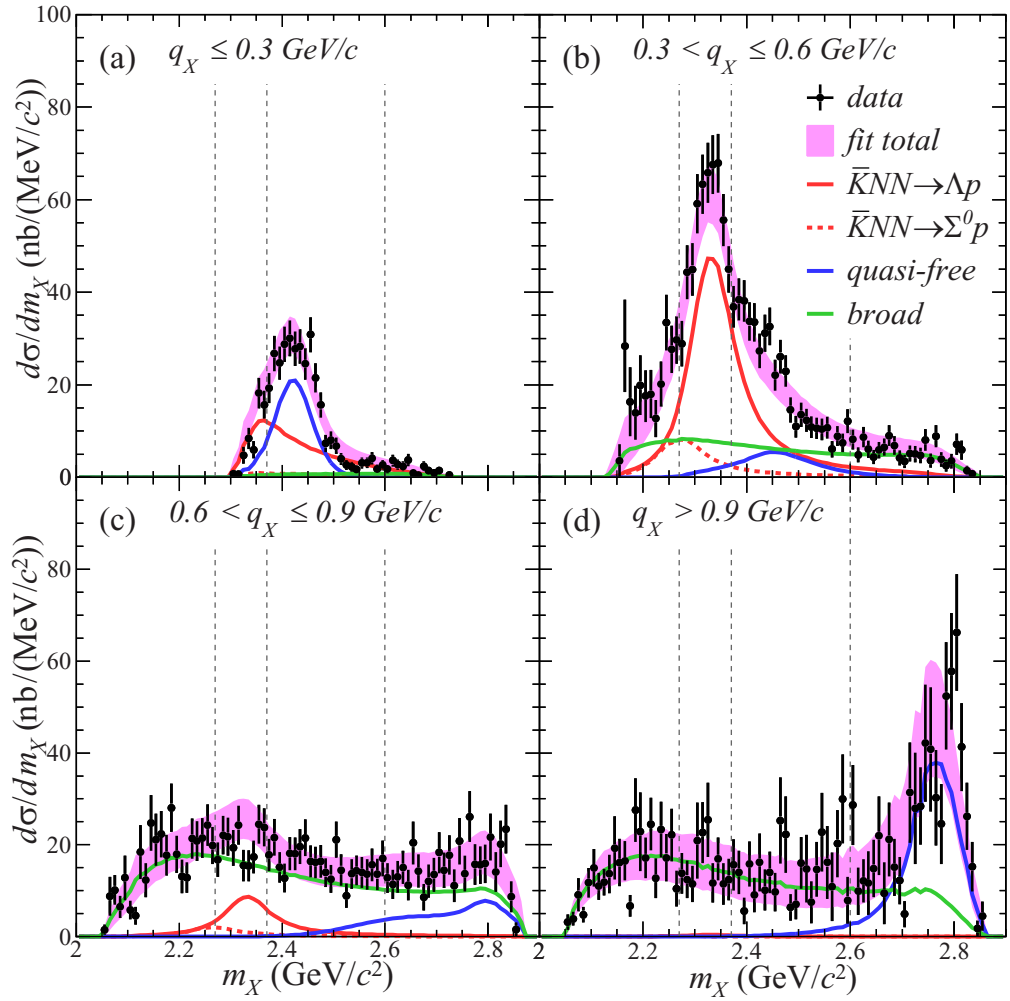

FIG. 10. m_X spectra for various intervals of q_X: (a) $q_X \leqslant 0.3$ GeV/c, (b) $0.3 < q_X \leqslant 0.6$ GeV/c, (c) $0.6 < q_X \leqslant 0.9$ GeV/c, and (d) 0.9 GeV/$c < q_X$. The dotted lines correspond to the m_X-slice regions given in Fig. 11.

2425 and 2234, respectively. We plotted the signal of $\bar{K}NN$ formation and its Λp decay as a red line, and $\bar{K}NN \to \Sigma^0 p$ in the Λpn-selection window as a red dashed line. To simplify the plot, we summed the $\mathrm{QF}_{\bar{K}-\mathrm{abs}}$ and broad contributions from the Λpn final state and from contaminations of the ΣNN final states, because the spectra for each reaction process are relatively similar [see Figs. 7(b) and 9]. As expected, the $\bar{K}NN$ formation signal is clearly seen in Fig. 10(b) in the m_X spectrum, and in Fig. 11(b) in the q_X spectrum.

At the lowest q_X region of the m_X spectrum in Fig. 10(a), the spectrum is confined in a medium mass region due to the kinematical boundary (see Figs. 4 and 5). In this region, the backward $\bar{K}$ part of the $\mathrm{QF}_{\bar{K}-\mathrm{abs}}$ process $K^- + N \to \bar{K} + n$ becomes dominant. In Fig. 10(b), the $\bar{K}NN$ formation signal is dominant and contributions from other processes, in particular the $\mathrm{QF}_{\bar{K}-\mathrm{abs}}$ process, are relatively suppressed. In the relatively large q_X region in Fig. 10(c), the broad component becomes dominant, while the $\bar{K}NN$ formation signal becomes weaker. At an even larger q_X region in Fig. 10(d), the forward $\bar{K}$ part of the $\mathrm{QF}_{\bar{K}-\mathrm{abs}}$ process becomes large, which distributes to the large m_X side. This events concentration may partially arise from direct K^- absorption on two protons in ^{3}He (2NA), but the width is too great to be explained by the Fermi motion. Therefore, it is difficult to interpret 2NA as the dominant process of this events concentration. In this q_X region, there is also a large contribution from the broad component.

Figure 11 shows the q_X spectra sliced on m_X. Figure 11(a) shows the region below the $\bar{K}NN$ formation signal where the broad distribution is dominant, having small leakage from the signal. As shown in the spectrum, the broad distribution has no clear structure and has a larger yield at a higher q_X region than at a lower q_X region. Figure 11(b) shows the $\bar{K}NN$ formation signal region, in which the events clearly concentrate at the lower q_X side. In Fig. 11(c), we can see the backward $\bar{K}$ part of the $\mathrm{QF}_{\bar{K}-\mathrm{abs}}$ process, together with the leakage from the signal and broad distribution. In contrast to $\bar{K}NN$, the $\mathrm{QF}_{\bar{K}-\mathrm{abs}}$ process even more strongly concentrates in the lower q_X region (neutron is emitted to the very forward direction). To compare the q_X dependence with that of the $\bar{K}NN$ formation

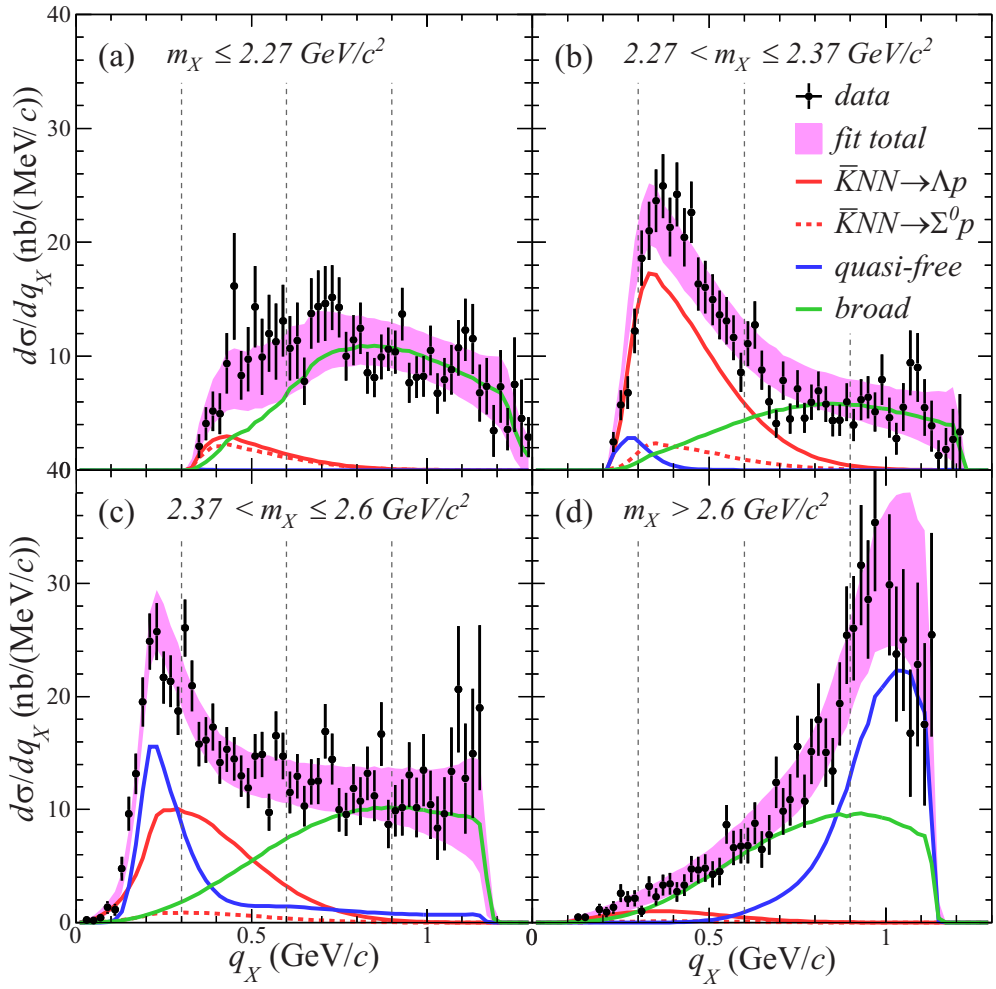

FIG. 11. q_X spectra for various intervals of m_X: (a) $m_X \leqslant 2.27$ GeV/c^2, (b) $2.27 < m_X \leqslant 2.37$ GeV/c^2, (c) $2.37 < m_X \leqslant 2.6$ GeV/c^2, and (d) 2.6 GeV/$c^2 < m_X$, with the fitting results shown as colored lines. The dotted lines correspond to the q_X-slice regions given in Fig. 10.

process, we formulated our model fitting function for the forward $\bar{K}$ $\mathrm{QF}_{\bar{K}-\mathrm{abs}}$ process to have a Gaussian form [see Eq. (10)]. The q_X spectrum at the highest m_X region is given in Fig. 11(d). The major components are the broad distribution and the forward $\bar{K}$ part of the $\mathrm{QF}_{\bar{K}-\mathrm{abs}}$ process. The centroid of the event concentration locates at an incident kaon momentum of 1 GeV/c, but the width in q is again too great to interpret it as being due to the 2NA reaction. Thus, the 2NA process would be rather small in the case of the Λpn final state of the present reaction.

To check the $\Sigma^0 pn$ contamination effect in the present fitting, we divided Fig. 10(b) into two regions for $m_{R^0} \leqslant m_n$ and $m_{R^0} > m_n$, as shown in Fig. 12. The figure shows that the spectra are consistent with the $\Sigma^0 pn$ final state distribution in Fig. 3(a), i.e., that the $\bar{K}NN \to \Sigma^0 p$ contribution exists only on the $m_{R^0} > m_n$ side. As shown in the figure, the m_X spectrum of Fig. 12(b) below the mass threshold of $M_{\bar{K}NN}$ is slightly wider and deeper than that of Fig. 12(a) in both the data and total fitting function, as expected, due to the presence of $\Sigma^0 pn$ contamination.

B. Fitted parameters

The converged 17 spectroscopic parameters are listed in Table II. We improved the fitting procedure to fully take into account the ΣNN final states in the present analysis, as well as the (m_X, q_X) dependence of the detector resolution. As a result, the values of the spectroscopic parameters were updated from our recent publication [24], though the updated values are within the error range of the previous publication.

The mass position of the $\bar{K}NN$ bound state M_K (or the binding energy $B_K \equiv M_{\bar{K}NN} - M_K$) and its decay width Γ_K are

$$M_K = 2.328 \pm 0.003(\mathrm{stat.})^{+0.004}_{-0.003}(\mathrm{syst.})\ \mathrm{GeV}/c^2$$
$$(B_K = 42 \pm 3(\mathrm{stat.})^{+3}_{-4}(\mathrm{syst.})\ \mathrm{MeV}),$$
$$\Gamma_K = 100 \pm 7(\mathrm{stat.})^{+19}_{-9}(\mathrm{syst.})\ \mathrm{MeV},$$

respectively. The S-wave Gaussian reaction form factor parameter of the $\bar{K}NN$ bound state Q_K is

$$Q_K = 383 \pm 11(\mathrm{stat.})^{+4}_{-1}(\mathrm{syst.})\ \mathrm{MeV}/c.$$

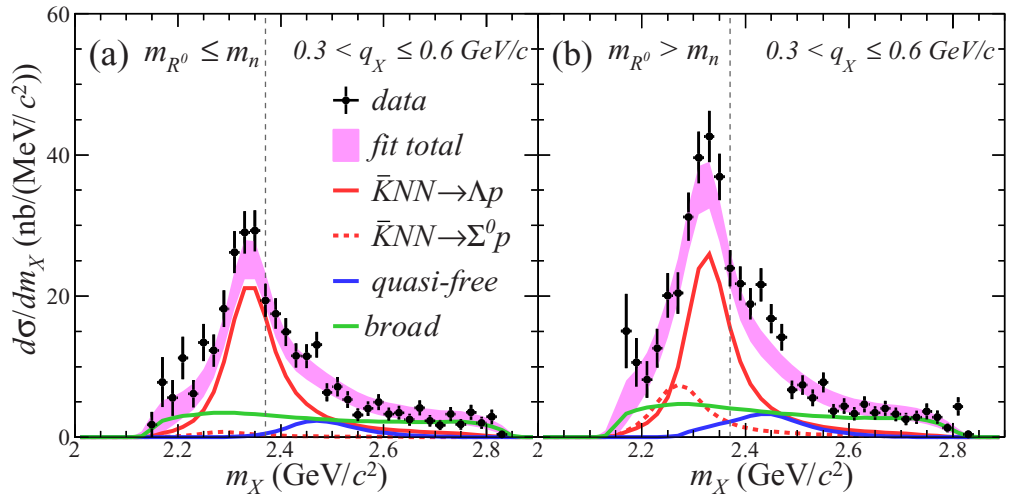

FIG. 12. m_X spectra for (a) $m_{R^0} \leqslant m_n$ and (b) $m_{R^0} > m_n$, with the fitting result. The selected q_X region is the same as for Fig. 10(b) ($0.3 < q_X \leqslant 0.6$ GeV/c). The vertical dotted line is $M_{\bar{K}NN}$. Note that the bin width is exceptional, $\Delta m_X = 20$ MeV/c^2, for these figures to have sufficient statistics.

The total production cross section of the $\bar{K}NN$ bound state going to the Λp decay mode $\sigma_K^{\rm tot} BR_{\Lambda p}$ was evaluated by integrating the spectrum to be

$$\sigma_K^{\rm tot} BR_{\Lambda p} = 9.3 \pm 0.8({\rm stat.})^{+1.4}_{-1.0}({\rm syst.})\ \mu{\rm b}.$$

In the present analysis, the strength of the $\bar{K}NN \to \Sigma^0 p$ decay mode is deduced based on the $\Sigma^0 pn$ contamination yield given by Fig. 3. By assuming that the relative yields of the three physical processes of ΣNN and those of Λpn are equal, we estimated the differential cross-section of $\bar{K}NN$ decaying into the $\Sigma^0 p$ mode $\sigma_K^{\rm tot} BR_{\Sigma^0 p}$ as

$$\sigma_K^{\rm tot} BR_{\Sigma^0 p} = 5.3 \pm 0.4({\rm stat.})^{+0.8}_{-0.6}({\rm syst.})\ \mu{\rm b}.$$

Therefore, the branching ratio of the Λp and $\Sigma^0 p$ decay modes was estimated to be $BR_{\Lambda p}/BR_{\Sigma^0 p} \sim 1.7$. The estimated branching ratio is higher than the value of the theoretical calculation based on the chiral unitary approach, predicting a ratio of almost one [30].

TABLE II. Converged 17 spectroscopic parameters and their errors.

$\bar{K}NN$ bound state	Value $\pm$ (stat.)$^{+}_{-}$(syst.)
A_0^K	$(1.523 \pm 0.103^{+0.001}_{-0.119}) \times 10^4$
M_K	$2.328 \pm 0.003^{+0.004}_{-0.003}$ GeV/c^2
Γ_K	$0.100 \pm 0.007^{+0.019}_{-0.009}$ GeV
Q_K	$0.383 \pm 0.011^{+0.004}_{-0.001}$ GeV/c
Nonmesonic QF$_{\bar{K}-{\rm abs}}$	Value $\pm$ (stat.)$^{+}_{-}$(syst.)
A_0^F	$(4.045 \pm 0.800^{+0.408}_{-0.953}) \times 10^4$
A_1^F	$(1.496 \pm 0.416^{+0.662}_{-0.456}) \times 10^2$
A_2^F	$(2.947 \pm 0.292^{+0.000}_{-2.947}) \times 10^{-39}$
σ_0	$0.045 \pm 0.004^{+0.006}_{-0.001}$ GeV/c^2
σ_2	$0.169 \pm 0.053^{+0.047}_{-0.037}$ GeV^{-1}
Q_F	$0.172 \pm 0.009^{+0.003}_{-0.005}$ GeV/c
m_0	$33.66 \pm 0.047^{+0.301}_{-1.641}$ MeV/c^2
q_0	$72.81 \pm 0.644^{+0.162}_{-9.590}$ MeV/c
Broad distribution	Value $\pm$ (stat.)$^{+}_{-}$(syst.)
A_0^B	$(0.596 \pm 2338^{+3767}_{-0.000}) \times 10^{-12}$
A_2^B	$(2.924 \pm 0.408^{+0.000}_{-0.104}) \times 10^3$
M_B	$2.128 \pm 0.032^{+0.013}_{-0.000}$ GeV/c^2
Γ_B	$0.532 \pm 0.068^{+0.000}_{-0.031}$ GeV
Q_B	$0.689 \pm 0.066^{+0.011}_{-0.001}$ GeV/c

C. Systematic errors

The systematic errors were evaluated by considering the uncertainties of the absolute magnetic field strength of the solenoid, the binning effect of spectra, and systematic errors of the branch of the final states (Table I). For production cross sections, we considered the luminosity uncertainty. To be conservative, the evaluated systematic errors are added linearly.

We succeeded in reproducing the data distribution by our model fitting functions. However, for the broad distribution, we cannot simply specify the physical process of its formation. Thus, we also tried an independent model fitting functions, which are intentionally unphysical but still able to reproduce the global data structure. A typical model fitting function fulfilling the requirements can be obtained by replacing the q_X-even polynomial term with a simple q_X-proportional one in Eq. (12). The q_X-proportional term is not physical by itself, and can only be possible as a comprehensive interference of an S wave and a P wave. As yet another extreme of the model fitting function of the broad distribution, we also examined a fit by replacing the Lorentzian term in Eq. (12) with a second-order polynomial. Although these alternative model functions are unphysical, we treated the centroid shifts of the other parameters as a source of systematic error for safety.

The systematic uncertainties are much reduced from Ref. [24], due to the improved analysis procedure by considering a precise and realistic evaluation of the ΣNN contamination in the Λpn-selection window.

D. Discussion

We introduced three physical processes to account for the data, *K*) $\bar{K}NN$, *F*) $\mathrm{QF}_{\bar{K}-\mathrm{abs}}$, and *B*) the broad distribution, and found that the presence of *K*) $\bar{K}NN$ is essential to explain the spectra self-consistently, which cannot be formed as an artifact. The presence of *F*) is naturally expected from the analysis on inclusive channel presented in Ref. [22], but the relative yield of the quasifree component is substantially reduced because we focused on the nonmesonic Λpn final state in the present paper. For process *B*), we pointed out that it could be due to pointlike 3NA kaon absorption, because the distribution is very broad. However, the weak but clear (m_X, q_X) dependence makes it difficult to simply interpret the broad component as 3NA.

For the $\bar{K}NN$ bound state, $B_K \sim 40$ MeV agrees nicely with phenomenological predictions [8,12,14,17,31]. However, it should be noted that the obtained B_K is the spectral Breit-Wigner pole position, neglecting the microscopic reaction dynamics in Eq. (2). Thus, the present Breit-Wigner pole might be different from the physical pole predicted by theoretical calculations.

$\Gamma_K \sim 100$ MeV is wide, as for a quasi-bound state, compared to the binding energy B_K. It is also wider than the $\Lambda(1405) \to \pi\Sigma$ decay width of ∼50 MeV (100%). If $\Lambda(1405)$ is the $\bar{K}N$ quasibound state, then it is naturally expected that the $\bar{K}NN \to \pi\Sigma N$ decay will occur in the same order as the *YN* decay channels.

As shown in Fig. 11(b), the production yield of the $\bar{K}NN$ bound state is much larger in a smaller q_X region. This trend is a common feature of nuclear bound-state formation reactions in general. In the $K^- + {}^3\mathrm{He} \to X + n$ formation channel, we can achieve a minimum momentum transfer to *X* as small as ∼200 MeV/*c*, which makes this channel the ideal formation process. However, $\sigma_K^{\mathrm{tot}} BR_{YN\,(=\Lambda p,\,\mathrm{or}\,\Sigma^0 p)}$ is still small compared to the total cross section of the elementary $K^- N \to \bar{K} n$ reaction by the order of $\mathcal{O}(10^{-3})$. Even if we take into account a mesonic decay branch similar to *YN* decay, the total $\bar{K}NN$ formation branch would still be less than $\mathcal{O}(10^{-2})$ of the elementary cross section. In spite of the small formation yield and large decay width near the binding threshold, we have succeeded in observing kaonic bound state formation. This is because the *YNN* final states, which strongly limit the number of possible complicated intermediate states such as mesonic processes, allow to trace the *s*-quark flow in the reaction. Moreover, the $\bar{K}NN$ signal and remaining non-mesonic $\mathrm{QF}_{\bar{K}-\mathrm{abs}}$ processes can be effectively separated by q_X slicing.

Let us consider the physical meaning of Q_K in Eq. (8). Q_K is quite large, more than twice the Q_F of the nonmesonic $\mathrm{QF}_{\bar{K}-\mathrm{abs}}$ process. The value of Q_F is natural in view of the size of the ^{3}He radius, as well as the strong angular dependence of the elementary process $K^- N \to \bar{K} n$ observed in Ref. [22] at $p_{K^-} = 1\,\mathrm{GeV}/c$, which is the primary reaction of Eq. (2). Instead, the value of Q_K may carry information on the spatial size of the $\bar{K}NN$ state. We formulated the model fitting function based on a simple PWIA calculation, assuming that the $\bar{K}NN$ wave function can be written in the ground state of a harmonic oscillator (HO). The spatial size of the HO wave function can be given as $R_K = \hbar/Q_K \sim 0.5$ fm (if we take into account the correction factor of the c.m. motion, $(2m_N + m_{\bar{K}})/2m_N$, $R_K \sim 0.6$ fm). The compactness is also naively supported by the large $B_K \sim 40$ MeV.

Finally, we briefly discuss the broad component. The present data show that the 2NA kaon absorption channels are weak, in contrast to kaon absorption at-rest experiments [32], so we need to understand why 3NA-like broad distribution still exists while the 2NA channels are weak. The distribution of this component f_B, given in Fig. 6(c), becomes a broad *P*-wave resonancelike structure characterized by M_B between $m_\Lambda + m_p$ and $M_{\bar{K}NN}$, $A_0^B << A_1^B$, as shown in Table II. This phenomenon might be simply due to the nature of the formula of the fitting function, given in Eq. (12), but it is worth studying experimentally in more detail to clarify the physics of this component. To be conservative, we kept our interpretation open with regard to the physical process of this broad distribution, and treated it as a source of systematic error.

Open questions still remain, such as the spin-parity J^P of the $\bar{K}NN$ state, and the relationship between the present $\bar{K}NN$ signal and $\Lambda(1405)$ resonance. Also, in the analysis, we have not taken into account the interference effects between the three introduced physical processes. More comprehensive studies are required to clarify these remaining questions.

V. SUMMARY

We have measured the Λpn final state in the in-flight reaction on a ^{3}He target at a kaon momentum of 1 GeV/*c*. We observed the kaonic nuclear quasibound state, $I_z = +1/2$ $\bar{K}NN$, and obtained its parameters by 2D fitting of the Λp invariant mass and momentum transfer.

The binding energy and the decay width of the state were $B_K = 42 \pm 3(\mathrm{stat.})^{+3}_{-4}(\mathrm{syst.})$ MeV and $\Gamma_K = 100 \pm 7(\mathrm{stat.})^{+19}_{-9}(\mathrm{syst.})$ MeV, respectively. The *S*-wave Gaussian reaction form factor was $Q_K = 383 \pm 11(\mathrm{stat.})^{+4}_{-1}(\mathrm{syst.})$ MeV/*c*. The total production cross sections of the $\bar{K}NN$ bound state decaying into nonmesonic Λp and $\Sigma^0 p$ modes were obtained to be $\sigma_K^{\mathrm{tot}} BR_{\Lambda p} = 9.3 \pm 0.8(\mathrm{stat.})^{+1.4}_{-1.0}(\mathrm{syst.})$ μb and $\sigma_K^{\mathrm{tot}} BR_{\Sigma^0 p} = 5.3 \pm 0.4(\mathrm{stat.})^{+0.8}_{-0.6}(\mathrm{syst.})$ μb, respectively. Thus, the ratio $\Lambda p/\Sigma^0 p$ decay branch was approximately 1.7.

Although it would be premature to make a conclusion regarding the spatial size of $\bar{K}NN$ from a simple PWIA-based model fitting function, the implied size is quite small compared to the mean nucleon distance in normal nuclei. However, the observed value of $Q_K = 383 \pm 11(\mathrm{stat.})^{+4}_{-1}(\mathrm{syst.})$ MeV/*c* is unexpectedly large (about twice as large as an elementary process), which makes the theoretical microscopic study difficult. Therefore, a more realistic theoretical calculation including detailed reaction dynamics and a more detailed experimental study are essential to understand the observed q_X distribution.

ACKNOWLEDGMENTS

The authors are grateful to the staff members of J-PARC/KEK for their extensive efforts, especially on the stable operation of the facility. We are also grateful to the

contributions of Professors Daisuke Jido, Takayasu Sekihara, Dr. Rie Murayama, and Dr. Ken Suzuki. This work is partly supported by MEXT Grants-in-Aid No. 26800158, No. 17K05481, No. 26287057, No. 24105003, No. 14102005, No. 17070007, and No. 18H05402. Part of this work is supported by the Ministero degli Affari Esteri e della Cooperazione Internazionale, Direzione Generale per la Promorzione del Sistema Paese (MAECI), StrangeMatter project.

[1] R. H. Dalitz and S. F. Tuan, Ann. Phys. (NY) **8**, 100 (1959).
[2] R. H. Dalitz, T. C. Wong, and G. Rajasekaran, Phys. Rev. **153**, 1617 (1967).
[3] K. Miyahara and T. Hyodo, Phys. Rev. C **93**, 015201 (2016).
[4] Y. Kamiya and T. Hyodo, Phys. Rev. C **93**, 035203 (2016).
[5] J. M. Hall, W. Kamleh, D. B. Leinweber, B. J. Menadue, B. J. Owen, A. W. Thomas, and R. D. Young, Phys. Rev. Lett. **114**, 132002 (2015).
[6] T. Yamazaki and Y. Akaishi, Phys. Lett. B **535**, 70 (2002).
[7] Y. Akaishi and T. Yamazaki, Phys. Rev. C **65**, 044005 (2002).
[8] Y. Ikeda and T. Sato, Phys. Rev. C **76**, 035203 (2007).
[9] N. V. Shevchenko, A. Gal, and J. Mareš, Phys. Rev. Lett. **98**, 082301 (2007).
[10] N. V. Shevchenko, A. Gal, J. Mareš, and J. Révai, Phys. Rev. C **76**, 044004 (2007).
[11] A. Doté, T. Hyodo, and W. Weise, Nucl. Phys. A **804**, 197 (2008).
[12] S. Wycech and A. M. Green, Phys. Rev. C **79**, 014001 (2009).
[13] A. Doté, T. Hyodo, and W. Weise, Phys. Rev. C **79**, 014003 (2009).
[14] Y. Ikeda and T. Sato, Phys. Rev. C **79**, 035201 (2009).
[15] N. Barnea, A. Gal, and E. Liverts, Phys. Lett. B **712**, 132 (2012).
[16] M. Bayar and E. Oset, Phys. Rev. C **88**, 044003 (2013).
[17] J. Révai and N. V. Shevchenko, Phys. Rev. C **90**, 034004 (2014).
[18] T. Sekihara, E. Oset, and A. Ramos, Prog. Theor. Exp. Phys. **2016**, 123D03 (2016).
[19] A. Doté, T. Inoue, and T. Myo, Phys. Rev. C **95**, 062201(R) (2017).
[20] S. Ohnishi, W. Horiuchi, T. Hoshino, K. Miyahara, and T. Hyodo, Phys. Rev. C **95**, 065202 (2017).
[21] A. Doté, T. Inoue, and T. Myo, Phys. Lett. B **784**, 405 (2018).
[22] T. Hashimoto *et al.*, Prog. Theor. Exp. Phys. **2015**, 61D01 (2015).
[23] Y. Sada *et al.*, Prog. Theor. Exp. Phys. **2016**, 051D01 (2016).
[24] S. Ajimura *et al.*, Phys. Lett. B **789**, 620 (2019).
[25] K. Agari *et al.*, Prog. Theor. Exp. Phys. **2012**, 02B009 (2012).
[26] K. Agari *et al.*, Prog. Theor. Exp. Phys. **2012**, 02B011 (2012).
[27] M. Iio *et al.*, Nucl. Instrum. Methods Phys. Res. A **687**, 1 (2012).
[28] K. L. Brown, F. Rothacker, D. C. Carey, and F. C. Iselin, TRANSPORT : a computer program for designing charged-particle beam-transport systems, Report number CERN-80-04, CERN Yellow Reports: Monographs (Geneva : CERN, 1980).
[29] A Kinematic Fit with Constraints [online], http://github.com/goepfert/KinFitter/wiki/KinFitter (2011).
[30] T. Sekihara, J. Yamagata-Sekihara, D. Jido, and Y. Kanada-En'Yo, Phys. Rev. C **86**, 065205 (2012).
[31] T. Yamazaki and Y. Akaishi, Phys. Rev. C **76**, 045201 (2007).
[32] R. Del Grande *et al.*, Eur. Phys. J. C **79**, 190 (2019).